Defect-driven Selective Metal Oxidation at Atomic Scale

Qi Zhu
Center of Electron Microscopy and State Key Laboratory of Silicon Materials, School of Materials Science and Engineering, Zhejiang University

Zhiliang Pan
Guilin University of Electronic Technology

Zhiyu Zhao
Zhejiang University

Langli Luo
Tianjin University https://orcid.org/0000-0002-6311-051X

Chaolun Ni
Zhejiang University

Hua Wei
Zhejiang University

Ze Zhang
Zhejiang University

Frederic Sansoz
University of Vermont https://orcid.org/0000-0002-2782-1832

Jiangwei Wang (jiangwei_wang@zju.edu.cn)
Zhejiang University https://orcid.org/0000-0003-1191-0782

Article

Keywords: defect-controlled reaction dynamics, atomic scale, nanoscale materials, crystal defects

Posted Date: July 16th, 2020

DOI: https://doi.org/10.21203/rs.3.rs-38564/v1

Version of Record: A version of this preprint was published at Nature Communications on January 25th, 2021. See the published version at https://doi.org/10.1038/s41467-020-20876-9.

Abstract

Nanoscale materials modified by crystal defects exhibit significantly different behaviours upon chemical reactions such as oxidation, catalysis, lithiation and epitaxial growth. However, unveiling the exact defect-controlled reaction dynamics (e.g. oxidation) at atomic scale remains a challenge for applications. Here, using in situ high-resolution transmission electron microscopy and first-principles calculations, we reveal the dynamics of a general site-selective oxidation behaviour in nanotwinned Ag and Pd driven by isolated stacking-faults and twin-boundaries. The coherent planar defects crossing the surface exhibit the highest oxygen binding energies, leading to preferential nucleation of oxides at these intersections. Fast diffusion of oxygen atoms along the planar-fault highways is shown to catalyse subsequent layer-by-layer inward oxide growth via atomic steps migrating on the oxide-metal interface. These findings provide an atomistic visualization of the complex reaction dynamics controlled by coherent planar defects in metallic nanostructures, which could enable the modification of physiochemical performance of nanomaterials through defect engineering.

Main Text

Nanotwinned materials possess a wide range of unprecedented mechanical and physical properties such as ideal maximum strength[1-3], excellent ductility[4], good fatigue resistance[5], high electrical conductivity[6], and exceptional thermal stability[7] due to the existence of coherent twin boundaries (TBs). With the advent of nanotechnology, TBs have also been revealed to critically influence the catalytic reactivity[8], electrochemical efficiency[9], growth dynamics[10], and oxidation rate[11, 12] of metallic nanomaterials, which can be ascribed to the change of both surface property (*e.g.,* coordination number, stress state and charge density) and internal lattice dynamics (*e.g.,* diffusion) by TBs. Since the reaction dynamics at TBs plays an important role in subsequent structural evolution and functionality of metallic nanomaterials[10, 12, 13], an atomic-scale understanding of this coherent defect contribution to chemical/electrochemical reactivity in nanomaterials is of general significance. However, in stark contrast to the well-established mechanistic insight into strengthening and softening mechanisms in nanotwinned materials[3, 14, 15], the atomistic origins of TB-assisted reactivity in nanotwinned materials have been largely elusive.

Recent studies on nanotwinned metallic nanoparticles attributed their superior catalytic performances to low-coordinated atomic steps, large tension, and high density of negative charges on the surface, which are critically affected by TBs[16-20]. These studies suggest that coherent TBs may act as preferential sites for selective chemical/electrochemical reactions and as channels for fast atom transport[19, 21]. Likewise, experimental studies have found that TBs significantly reduce the energy barriers for growth[13], mass transport[9], and solid-state reaction[22]. On the contrary, the twin-modified surface structures were reported to enhance the resistance to corrosion and oxidation in nanotwinned metals, compared with their twin-free nanocrystalline counterparts[12, 23]. Therefore, the critical influence of TBs on the chemical response of metallic materials under different environments is still under debate. To date, however, systematic

investigations of the defect-assisted oxidation dynamics at the atomic scale remain challenging in practice.

Here, we study the oxidation dynamics of nanotwinned metallic nanocrystals in atomistic detail by conducting integrated in situ transmission electron microscopy (TEM) characterizations and density-functional-theory (DFT) based *ab initio* calculations. The results expose a unique site-selective oxidation behaviour in nanotwinned silver (Ag) and palladium (Pd), where coherent crystal defects including TBs and stacking-faults (SFs) strongly favour surface oxygen binding and accelerate oxide nucleation and growth. Subsequent inward growth of the oxide is promoted by the fast diffusion of oxygen along TB and SF highways that intersect with the oxide/matrix interface, leading to a layer-by-layer oxide growth mechanism. Furthermore, we qualitatively validate this defect-assisted oxidation kinetics in air over largely different time scales spanning from few seconds to several days. These findings provide atomistic insights into the defect-assisted reaction dynamics of nanoscale metals, which has direct ramifications for the development of advanced nanomaterials through defect engineering.

Selective oxidation of nanotwinned Ag along isolated TBs and SFs

In contrast to the widely reported oxidation of nanosized FCC metals (*e.g.,* Cu and Pd) from the {111} and {100} facets[24-26], our *in situ* experiments unambiguously demonstrate preferential oxide nucleation at the TB-surface junction, even in the presence of numerous low energy (111) facets on the nearby surface. As shown in Fig. 1a, the as-fabricated Ag nanocrystal consists of a straight TB along the axial direction, which is confirmed by the fast Fourier transform (FFT) pattern in Fig. 1f. Upon oxidation, sequential images clearly show that an oxide embryo preferentially nucleates at the twinned tip (Fig. 1b), although the lattice structure of this as-formed oxide embryo cannot be quantitatively identified. After 88 s, recognizable lattices appear as the oxide grows continuously inward along the TB (Fig. 1c). Meanwhile, the oxide expands laterally to form an asymmetrical conical cap sitting on top of the nanocrystal (Fig. 1d). No oxidation was detected on {111} facets away from the TB[24-26], suggesting a strong site selection upon oxidation of the nanotwinned tip. A close-up high-resolution TEM image is presented in Fig. 1e to show the atomistic structure of the Ag_2O product above the Ag matrix at the tip. The interface is atomically sharp with one atomic (111) step. The corresponding FFT patterns (Fig. 1g) further confirm the as-formed oxide of Ag_2O with a lattice constant of a = 4.718 Å (Space group: $Pn3m$), which bears a specific orientation relation with the Ag matrix as $(1\ 0)_{Ag}//(100)_{Ag2O}$ and $(11\ )_{Ag}//(010)_{Ag2O}$. It is further observed that oxidation along the TB always precedes that of the neighbouring lattices, as shown in Fig. 1e, which indicates evident TB-assisted oxidation. The selective oxidation mechanism is more conspicuous during the subsequent growth of this oxide layer, because the thickness of oxide (along axial direction) decreases gradually from ~4.3 nm at the tip down to almost zero at free surfaces on both sides (Fig.1d). It is noted that no other defect activity is observed throughout the oxidation process of this Ag twinned tip.

Atomic-level snapshots in Fig.1i-j further emphasize the preferential oxide nucleation at the TB-surface junction. A zoomed-in image shows the atomic structure of the clean Ag nanocrystal, which exposes two

conjugate (111) surfaces with multiple atomic kink steps very close to the TB-surface junction, while a high density of alternate (111) and (11) atomic facets dominate both sides of the surface away from the TB (Fig. 1h). The oxygen atoms are preferentially adsorbed to the surface layer of Ag near the TB (shown by the blurred profile of the top surface in Fig. 1i), which induces a slight lattice distortion visible in the sub-surface layers. In contrast, the faceted morphology of the surface away from the TB is generally retained, indicating significantly less oxygen adsorption on these low energy facets. Eventually, the adsorbed oxygen accumulating at the TB-surface junction incubates an oxide nucleus with an average height of 4.8 Å (Fig. 1j), which is favourably located on the (11) surface facet with the largest number of kink steps. With prolonged oxidation, the Ag_2O layer simultaneously grows inward along the TB and expands laterally along conjugate (11) surface facets (Fig. 1k).

The above experiment demonstrates a TB-assisted site-specific oxidation behaviour in an Ag nanocrystal, which dominates over those widely reported low-energy surface facets for the nucleation and growth of oxides[24-26]. This unique behaviour is further validated in additional examples of Ag nanocrystals with an axial TB (see Supplementary Fig. 1), where the TB-surface junction serves as a universally preferential nucleation site for oxide embryos, accompanied by oxide growth along the TB. Similar oxidation behaviours are also observed in other FCC metallic nanocrystals, *e.g.* Pd, with significantly higher SF energy (Supplementary Figs. 2-4). This common site-selective nucleation and TB-assisted growth of oxide clearly indicate that an isolated TB can effectively promote the oxidation of FCC metals, which markedly differs from the suppressed chemical reactivity of nanotwinned Cu nanowires reported previously[27].

Furthermore, this phenomenon was found to occur with isolated TBs positioned away from the Ag tip (see Supplementary Fig. 5), which suggests that the TB effect is intrinsic. DFT-based atomistic simulations were performed to quantitatively confirm our hypothesis by calculating the Ag-O surface binding energy (E_b), which decouple the intrinsic influence of TB from other atomic surface steps. We first constructed a twinned Ag tip (consistent with our experiments) with a junction between a vertically aligned coherent TB and two perfectly smooth (11) conjugate surfaces. These calculations reveal that the O interstitial site closest to the TB possesses the highest Ag-O surface binding energy E_b = 3.931 eV, compared with E_b = 3.807 eV at the equivalent interstitial site on the (11) surface of the single crystal farther away from TBs (Fig. 2a-b). Therefore, oxide nucleation should preferentially occur at the TB-surface junctions, which matches perfectly with our experimental observations. Furthermore, we find that the Ag-O binding energy at a kink step on the (111) surface is considerably increased from E_b = 3.897 eV (Fig. 2c) to E_b = 4.078 eV in the vicinity of a planar SF (Fig. 2d). These theoretical results are significant in two aspects. First, the DFT calculations quantitatively prove that both isolated TBs and SFs give rise to stronger surface binding of O atoms. Second, it has been reported that twinning creates low-coordinated sites to which dioxygen preferentially bonds at TB-surface junctions in nanotwinned metals[28], suggesting that the O reactivity of surface atoms maybe directly relate to their coordination number (CN). However, our DFT-based calculations demonstrate that the coordinate number (CN) of atoms at the TB-surface junction (CN=8) is larger than that at the edge of a (111) kink step (CN=7), see black-coloured atoms in

Fig. 2c and inset of Fig. 2e, respectively, clarifying the predominant role of binding energy in selective oxide nucleation at the TB-surface junction, in contrast to the CN-governed surface reactivity reported in literature[28].

Oxidation efficiency as a function of defect configuration and spacing

Analogous to the strong twin-size dependence of mechanical behaviour in nanotwinned metals[1-3], it is significant to study how the chemical reactivity and oxidation could vary with TB spacing, because smaller twins are frequently observed to reduce the reactivity via surface modification[12]. To this end, despite the technical difficulties in controlling TB spacing experimentally, DFT calculations are used to quantify the mean oxygen binding energy averaged over multiple O interstitial sites of different defect-modified surface configurations, as shown in Fig. 2e and Supplementary Figs. 6-9. Specifically, we compute the mean binding energy of different nanotwins (NTs) with a constant TB spacing varied from 4.8 Å to 28.8 Å, in comparison to that of two single-crystal configurations containing either an isolated SF or no imperfection (SGL). The surface intersecting either TB or SF is composed of zig-zag low-energy (111) and (001) facets (insets of Fig. 2e). For consistency, the perfect single-crystal configuration was constructed with the same type of zig-zag facets. Fig. 2e shows that the mean O binding energy (E_b) of NTs is noticeably higher than that of the perfect single crystal, which agrees with the experimental observations (Fig. 1). However, the binding energy tends to decrease as the TB spacing is reduced, which is in good agreement with the uniform and slower oxide growth observed in regions of copper nanowires containing highly dense and evenly spaced nanotwins[12, 27]. Even more remarkably, the average E_b at an isolated SF reaches 3.981 eV, which surpasses those of NTs with any size.

Additional experiments in samples with different planar defects further confirm the strong site-selective and defect-assisted surface oxidation in Ag and Pd nanocrystals, as shown in Fig. 3 and Supplementary Figs. 4-5. Specifically, Fig. 3a-d gives clear evidence for the SF-assisted oxidation in Ag nanocrystals with an isolated SF. A pre-existing SF laid almost perpendicular to the [111] axial direction of the Ag nanocrystal (Fig. 3a), intersecting the nanocrystal surfaces on both sides. A close-up image in the inset shows that the surface is oriented almost perfectly parallel to the (112) plane, albeit some (111) kink steps exist on the other side of the surface-SF junction. Upon initial oxidation, two oxide embryos nucleate simultaneously at the SF-surface junctions on both sides (Fig. 3b). This observation agrees well with the highest O binding energy at SF predicted by DFT. Moreover, the oxide embryo is followed by inward growth along the SF (Fig. 3c-d) similarly to our previous observations at isolated TBs, where the average oxidation rate (along the SF) is calculated to be ~ 0.07 nm s^{-1} (Supplementary Fig. 10).

To further confirm the DFT predictions that the O binding energy is higher at SFs than in TBs, *in situ* oxidation experiments were conducted on an Ag nanocrystal containing both pre-existing SF and multiple parallel TBs with uneven spacing, as shown in Fig. 3e-h. The surface structure was almost identical near the intersection sites with SF and TB (Fig. 3e), which makes the influence of interface facets negligible in this configuration. An oxide embryo preferentially nucleates at the SF-surface junction located between two TBs (TB3 and TB4 with a spacing of 1.88 nm), connecting a large twin to one of the smallest twins

(Fig. 3f). It is worth noting, however, that no observable oxidation occurs at the nearby surface intersected by twins. Subsequent inward growth of this oxide island preferentially proceeds along the SF (Figs. 3g and 3h), suggesting that SF is a fast pathway for oxygen diffusion. Associated with the inward oxide growth is the lateral expansion of the oxide along the surface facets (consistent with that at the surface-TB junction), which leads to a spindle-shaped oxide. In summary, strong site-selection dictates the defect-assisted surface oxidation in metallic nanocrystals containing multiple TBs and SFs, and the general significance of coherent planar defects as fast pathways for oxygen diffusion is unambiguously demonstrated (see additional example in Supplementary Fig. 11).

Defect-assisted oxidation mechanism and kinetics

Figure 4a-d presents a series of TEM snapshots showing the atom-level dynamics of TB-assisted oxide growth during the twinned tip experiment in Fig. 1. Upon nucleation, the interface between Ag nanocrystal and as-formed Ag_2O consists of six single-atom steps (Fig. 4a). For the next second, the pre-existing steps are observed to migrate laterally along the Ag/Ag_2O interface, away from the TB, while the atoms at the TB tip react into Ag_2O, forming a pair of new steps (7 and 8) in a sub-layer (Fig. 4b). This specific event suggests that interstitial O atoms are more rapidly diffused along the TB defect to bind with freshly exposed Ag atom columns, as will be discussed below. During the following seconds, each newly formed step moves away on the Ag/Ag_2O interface (Fig. 4c) and gives space for the formation of new Ag_2O lattices into sub-layers initiated from the TB (Fig. 4d). This layer-by-layer oxide growth is similar to the growth of CuO nanowires assisted by (002) TBs[13], and eventually leads to a conical oxide cap on the Ag nanocrystal (Fig. 1d).

The layer-by-layer growth mechanism is schematically illustrated in Fig. 4e, where the TB atoms in the top Ag layer and atomic steps on the Ag/Ag_2O interface naturally possess a lower CN than those in the perfect FCC lattice (CN = 12). In fact, our DFT calculations have indicated that the CN of FCC Ag atoms decreases to CN = 10 at an Ag/Ag_2O interface (Supplementary Fig. 12). Therefore, these low-coordinated Ag atoms at the oxide interface favour oxygen binding and induce a ledge flow mechanism at the reaction front[29], which is supported by experimental evidence (Fig. 4a-d). Furthermore, the surface oxide on the nanotwinned tip is observed to grow continuously and sequentially, suggesting that the coupled axial and lateral propagation of the Ag/Ag_2O interface arises from fast diffusion of O atoms along the TB[30]. Similar TB-assisted diffusion has been reported in SnO_2 nanowire for Li ions (during lithiation)[9] and in α-Ti for O interstitials[31]. Also, the same evidence of TB-assisted layer-by-layer oxidation dynamics was found in our additional experiments of nanotwinned Pd, as exemplified in Supplementary Fig. 3.

The time-dependent oxidation kinetics along the TB is quantified in Fig. 4f. The TB-assisted oxidation of Ag nanocrystal (shown in Fig. 1) can be divided into three stages, *i.e.,* fast nucleation, steady growth, and self-limiting equilibrium. During the fast nucleation ($t \leq 80$ s), an oxide embryo nucleates by adsorption of rarefied O atoms from the ultrahigh vacuum chamber of TEM. Our DFT calculations have predicted intrinsic TB and SF effects that yield a substantial increase in the surface binding energy of oxygen in Ag

nanocrystals. Quantitative analysis in inset 1 of Fig. 4f confirms this theory by revealing that the axial oxidation depth *L* (along TB) during the nucleation period is linear as a function of time. A linear rate of reaction is commonly associated with initial fast oxidation observed on a number of metals at low temperatures[32]. Subsequently, inward growth of the oxide proceeds layer-by-layer assisted by the TB (Fig. 4e), which is referred to as the steady growth stage (80 s < t < 200 s). Our quantitative study in inset 2 of Fig. 4f shows that the oxide growth kinetics follows a logarithmic law during steady growth. Direct logarithmic kinetics is usually derived from electron tunnelling and ionic O^- flow in very thin oxide films[32]. However, the observation of spindle-shaped oxide islands (see Fig. 3 and Supplementary Fig. 2) indicates that oxygen diffusivity along TBs in the thin oxide layer is enhanced in comparison to the diffusivity on standard {111} FCC planes, which agrees well with recent DFT calculations[31]. Meanwhile, the high oxygen concentration radiates from the TB to propel the lateral flow of newly formed steps along the low-coordinated Ag/Ag_2O reaction front. As the oxide thickness grows to ~ 10 nm, however, few O ions are pumped towards the oxidation front. Consequently, the reaction front tends to be short of O supply, and the oxide growth rate is gradually reduced. This process is self-limiting under our experimental condition, because oxygen is rare in the vacuum of the microscope. A similar oxidation trend is observed for an isolated SF as well (Supplementary Fig. 10).

It is established that pre-existing surface steps and lattice defects can facilitate diffusion and chemical reaction in defective metallic nanocrystals[21, 25]. When the defect density increases, the surface strain may change markedly[16, 18-20], resulting in some unique properties, such as enhanced oxidation of metallic nanoparticles due to strain-mediated ion transport[33]. The presence of TBs can also change the properties of neighbouring surfaces[27]. In addition, twinning could induce large surface tension and highly negative charge density[18, 19] that may also favour O adsorption. In contrast to nanotwinned Ag, however, we found that homogeneous oxidation initiates from multiple sites simultaneously in defect-free Ag single crystals (Supplementary Fig. 13); such process is mainly dominated by surface diffusion rather than defect-assisted diffusion, leading to significantly slower kinetics and reduced inward growth. This comparison points to the conclusion that in nanocrystals containing coherent planar defects, the chemical reactivity under different conditions is not only controlled by the nucleation kinetics, but also critically limited by the subsequent growth kinetics[32].

Despite the exceptional chemical inertness of bulk Ag and Pd, nanosized noble metals are inherently vulnerable to oxidation, which probably originates from the increased specific surface area. Under electron beam irradiation, the binding of O with metallic atoms could be significantly facilitated at room temperature[34, 35], even under low oxygen partial pressure in the ultrahigh vacuum TEM column (~2.5 10^{-7} Torr). Due to the high thermal conductivity of Ag (429 W mK^{-1}) and Pd (72 W mK^{-1}), temperature rise induced by the electron beam should be negligible in Ag and Pd nanocrystals[36]. However, the electron beam could also alter chemical bonds in the sample and induce ionization of gas molecules[37], thereby catalysing chemical reactions (*e.g.*, oxidation). To exclude any possible beam effects on oxidation, nanotwinned Ag (fabricated with the same method) with multiple pre-existing TB and SF, was exposed in

air at room temperature for 48 hours. The TEM image captured after oxidation (Fig. 5) shows that the naturally oxidized nanotwinned Ag exhibits similar site-selective oxidation along pre-existing isolated SFs, where negligible oxide was formed at defect-free areas (Fig. 5). This experiment provides qualitative evidence for the insensitivity of site-selective oxidation to the electron beam irradiation and oxygen concentration, as well as to the time scale for oxidation.

Conclusion

In situ atomic-scale observations and DFT calculations have revealed a site-selective preferential oxidation behaviour in nanotwinned metals at isolated planar defects including TBs and SFs. Such unique behaviour originate from the synergistic high binding energy at the TB/SF-surface junctions and enhanced diffusion kinetics along TBs and SFs in metals with uneven twin sizes. This defect-assisted surface oxidation mechanism in metallic nanocrystals indicates the general significance of the coupling between nucleation kinetics and subsequent growth dynamics upon chemical reactions, deconstructing the relations between atomic-scale defects and physicochemical phenomena at the nanoscale. Given that nanoscale twins are common in a variety of nanostructured materials[16-20, 38], this site-selective mechanism should play important roles during the nanowire growth, catalytic/chemical/electrochemical reactions and solid-state phase transformation in nanotwinned materials[16-20, 38]. Therefore, our findings of atomistic reaction dynamics of defective nanaocrystals hold fundamental and technological ramifications for the development of advanced nanomaterials through defect engineering.

Methods

***In situ* TEM oxidation.** *In situ* oxidation experiments were performed in a FEI Titan G^2 60-300 transmission electron microscope operated at 300 kV equipped with a single-tilt STM-TEM holder from Zeptools Co. Before *in situ* oxidation experiments, Ag and Pd rods (0.25 mm in diameter, 99.99 wt.% purity, ordered from Alfa Aesar Inc.) were mechanically fractured using a ProsKit wire cutter to obtain a clean fracture surface with numerous nanoscale tips. Due to the severe plastic deformation in the fracture zone, numerous nanoscale twins were induced in the nanotips on the fracture surface. Then, an Ag or Pd rod was loaded on to the TEM holder. To characterize the twin structure, nanoscale tips in the <110> zone axis were selected for the *in situ* oxidation experiments. Then, *in situ* oxidation experiments were conducted at room temperature under ultra-high vacuum (UHV) atmosphere 2.5 10^{-7} Torr (corresponding to an oxygen partial pressure of ~5 10^{-8} Torr) to characterize the oxidation dynamics at an atomic scale. The extremely low oxygen pressure in the TEM chamber is sufficient to induce evident oxidation of the nanoscale metal. Besides, some oxygen may be pre-absorbed on the fracture surface of Ag and Pd rods. In all experiments, the TEM was operated at 300 kV with a low electron beam current density of ~100 A s^{-1} to minimize the possible beam effects. To investigate the oxidation dynamics, a CCD camera was used to record all experiments in real time at a rate of ~0.3 s per frame.

First-principles calculations. *Ab initio* calculations were performed using the Vienna *ab initio* simulation package (VASP) implemented based on the Kohn-Sham density functional theory[39]. Plane-wave basis set was used to expand the Kohn-Sham orbitals with an energy cutoff of 450 eV. The exchange-correlation functional was in the form of generalized gradient approximation developed by Perdew, Burke, and Ernzerhof (PBE)[40]. The projector augmented plane wave method (PAW) pseudopotential was used to reduce the number of plane waves near the nucleus. Geometry optimization was performed to calculate the local minimum potential energy of each atomic configuration, where the ion positions were updated until the maximum force acting on the atoms was less than 1×10^{-4} eV Å $^{-1}$. Since the simulation cell was large enough in X and Y direction, but only ~6 Å in Z direction, k-point calculation within a mesh of 1×1×3 was performed for the wavefunction optimization with a convergence criterion of 1×10^{-6} eV. The O binding energy, i.e. the energy required to remove one O atom from its bonded matrix configuration was calculated such as

$$E_{\mathrm{Binding}}^{\mathrm{O}} = E_{\mathrm{ISO}}^{\mathrm{O}} + E_{\mathrm{Matrix}}^{\mathrm{Ag}} - E_{\mathrm{Matrix}}^{\mathrm{Ag,O}},$$

where

$$E_{\mathrm{ISO}}^{\mathrm{O}},\ E_{\mathrm{Matrix}}^{\mathrm{Ag}},\ E_{\mathrm{Matrix}}^{\mathrm{Ag,O}}$$

are the potential energy of an isolated O atom, that of the pure Ag configuration without O atom, and that of the same Ag configuration bonded with a surface O atom, respectively. For each Ag model, we studied between 2 and 6 different interstitial positions of surface O bond, see Supplementary Materials.

References

1. Lu, L., Chen, X., Huang, X. & Lu, K. Revealing the Maximum Strength in Nanotwinned Copper. *Science* **323**, 607-610 (2009).

2. Wang, J. *et al.* Near-ideal theoretical strength in gold nanowires containing angstrom scale twins. *Nat. Commun.* **4**, 1742 (2013).

3. Ke, X. *et al.* Ideal maximum strengths and defect-induced softening in nanocrystalline-nanotwinned metals. *Nat. Mater.* **18**, 1207-1214 (2019).

4. Wei, Y. *et al.* Evading the strength–ductility trade-off dilemma in steel through gradient hierarchical nanotwins. *Nat. Commun.* **5**, 3580 (2014).

5. Pan, Q. *et al.* History-independent cyclic response of nanotwinned metals. *Nature* **551**, 214-217 (2017).

6. Lu, L. *et al.* Ultrahigh Strength and High Electrical Conductivity in Copper. *Science* **304**, 422-426 (2004).

7. Huang, Q. *et al.* Nanotwinned diamond with unprecedented hardness and stability. *Nature* **510**, 250-253 (2014).

8. Sun, X. *et al.* Crystalline Control of {111} Bounded Pt3Cu Nanocrystals: Multiply-Twinned Pt3Cu Icosahedra with Enhanced Electrocatalytic Properties. *ACS Nano* **9**, 7634-7640 (2015).

9. Nie, A. *et al.* Twin Boundary-Assisted Lithium Ion Transport. *Nano Lett.* **15**, 610-615 (2015).

10. Lim, B. *et al.* Twin-Induced Growth of Palladium–Platinum Alloy Nanocrystals. *Angew. Chem. Int. Ed.* **121**, 6422-6426 (2009).

11. Nishimoto, K. *et al.* Fast Oxidation of Porous Cu Induced by Nano-Twinning. *Inorg. Chem.* **57**, 2908-2916 (2018).

12. Huang, C.-L., Weng, W.-L., Liao, C.-N. & Tu, K. N. Suppression of interdiffusion-induced voiding in oxidation of copper nanowires with twin-modified surface. *Nat. Commun.* **9**, 340 (2018).

13. Rackauskas, S. *et al.* In situ study of noncatalytic metal oxide nanowire growth. *Nano Lett.* **14**, 5810-5813 (2014).

14. Lu, K., Lu, L. & Suresh, S. Strengthening Materials by Engineering Coherent Internal Boundaries at the Nanoscale. *Science* **324**, 349 (2009).

15. Jang, D., Li, X., Gao, H. & Greer, J. R. Deformation mechanisms in nanotwinned metal nanopillars. *Nat. Nanotech.* **7**, 594-601 (2012).

16. Wang, L. *et al.* Aerobic Oxidation of Cyclohexane on Catalysts Based on Twinned and Single-Crystal Au75Pd25 Bimetallic Nanocrystals. *Nano Lett.* **15**, 2875-2880 (2015).

17. Tang, Y. & Ouyang, M. Tailoring properties and functionalities of metal nanoparticles through crystallinity engineering. *Nat. Mater.* **6**, 754-759 (2007).

18. Zhang, X. *et al.* Nanoporous twinned PtPd with highly catalytic activity and stability. *Journal of Materials Chemistry A* **3**, 2050-2056 (2015).

19. Yin, A.-X. *et al.* Multiply twinned Pt–Pd nanoicosahedrons as highly active electrocatalysts for methanol oxidation. *Chem. Commun.* **48**, 543-545 (2012).

20. Lim, B. *et al.* Twin-Induced Growth of Palladium-Platinum Alloy Nanocrystals. *Angew. Chem. Int. Ed.* **48**, 6304-6308 (2009).

21. Zhou, G. *et al.* In situ atomic-scale visualization of oxide islanding during oxidation of Cu surfaces. *Chem. Commun.* **49**, 10862-10864 (2013).

22. Tang, W. *et al.* Nucleation and Atomic Layer Reaction in Nickel Silicide for Defect-Engineered Si Nanochannels. *Nano Lett.* **13**, 2748-2753 (2013).

23. Zhao, Y., Cheng, I. C., Kassner, M. E. & Hodge, A. M. The effect of nanotwins on the corrosion behavior of copper. *Acta Mater.* **67**, 181-188 (2014).

24. Todorova, M., Reuter, K. & Scheffler, M. Density-functional theory study of the initial oxygen incorporation in Pd (111). *Physical Review B* **71**, 195403.1-195403.8 (2005).

25. Zhou, G. W. *et al.* Step-Edge-Induced Oxide Growth During the Oxidation of Cu Surfaces. *Phys. Rev. Lett.* **109**, 235502.1-235502.5 (2012).

26. Li, L. *et al.* Surface-Step-Induced Oscillatory Oxide Growth. *Phys. Rev. Lett.* **113**, 136104.1-136104.5 (2014).

27. Huang, C.-L. & Liao, C.-N. Chemical reactivity of twin-modified copper nanowire surfaces. *Appl. Phys. Lett.* **107**, 021601 (2015).

28. Krajčí, M., Kameoka, S. & Tsai, A.-P. Twinning in fcc lattice creates low-coordinated catalytically active sites in porous gold. *J. Chem. Phys.* **145**, 084703 (2016).

29. Liu, X. H. *et al.* In situ atomic-scale imaging of electrochemical lithiation in silicon. *Nat. Nanotech.* **7**, 749-756 (2012).

30. Sutton, A. P. & Balluffi, R. W. *Interfaces In Crystalline Materials* (Oxford Univ. Press, Oxford, 1996).

31. Hooshmand, M. S., Niu, C., Trinkle, D. R. & Ghazisaeidi, M. First-principles prediction of oxygen diffusivity near the (10 2) twin boundary in titanium. *Acta Mater.* **156**, 11-19 (2018).

32. Lawless, K. R. The oxidation of metals. *Rep. Prog. Phys.* **37**, 231 (1974).

33. Pratt, A. *et al.* Enhanced oxidation of nanoparticles through strain-mediated ionic transport. *Nat. Mater.* **13**, 26-30 (2014).

34. Zheng, H. *et al.* Direct atomic-scale observation of layer-by-layer oxide growth during magnesium oxidation. *Appl. Phys. Lett.* **104**, 141906 (2014).

35. Oh, S. H. *et al.* Oscillatory Mass Transport in Vapor-Liquid-Solid Growth of Sapphire Nanowires. *Science* **330**, 489-493 (2010).

36. Egerton, R. F., Li, P. & Malac, M. Radiation damage in the TEM and SEM. *Micron* **35**, 399-409 (2004).

37. Hansen, T. W. & Wagner J. B. *Controlled Atmosphere Transmission Electron Microscopy* (Springer, Switzerland, 2016).

38. Algra, R. E. *et al.* Twinning superlattices in indium phosphide nanowires. *Nature* **456**, 369-372 (2008).

39. Kresse, G. & Furthmüller, J. Efficient iterative schemes for ab initio total-energy calculations using a plane-wave basis set. *Phys. Rev. B* **54**, 11169-11186 (1996).

40. Perdew, J. P., Burke, K. & Ernzerhof, M. Generalized Gradient Approximation Made Simple. *Phys. Rev. Lett.* **77**, 3865-3868 (1996).

Declarations

Acknowledgements

J.W. acknowledges the support of the National Natural Science Foundation of China (51771172 and 51701179). Z.P. and F.S. are grateful for the support from the US Department of Energy (DOE) (grants no. DE-SC0016270 and no. DE-SC0016270) and the supercomputer Cori of the National Energy Research Scientific Computing Centre, supported by DOE contract no. DE-AC02-05CH11231.

Author contributions

J.W. and F.S. conceived and guided the research. J.W., Z.Z., Q.Z., and N.C. designed, conducted, and analysed the experiments. Z.P. and F.S. developed, performed and analysed the DFT simulations. L.L., H.W. and Z.Z. helped with data analysis. J.W., F.S. and Q.Z. prepared the manuscript. All authors contributed to the data discussion and manuscript revision.

Competing interests

The authors declare no competing interests.

Figures

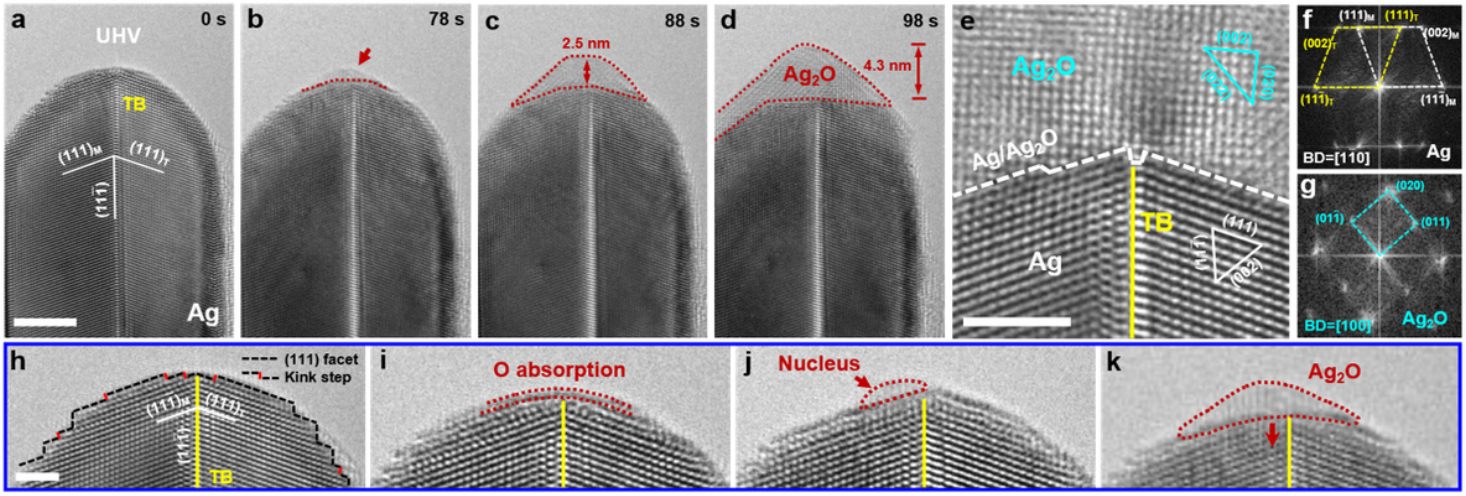

Figure 1

Twin boundary-favoured oxidation of Ag nanocrystal. (a) Pristine Ag nanocrystal with a pre-existing twin boundary (TB) along the axial direction, which was placed in the ultrahigh vacuum (UHV) column of the transmission electron microscope (TEM). The nanocrystal has a clean surface with dominant (111) facets. (b-d) Dynamic snapshots showing the oxidation process of the Ag nanocrystal. The oxide embryo preferentially nucleated at the TB-surface junction (b), which grew continuously along the TB and expanded laterally on the nanocrystal surface (c-d). The red dotted line delineates the oxidized area. (e) Zoomed-in image showing the atomistic structure of the Ag2O oxide (top) and the Ag matrix (bottom). (f-g) Fast Fourier transform (FFT) patterns of the Ag nanocrystal with an axial TB and the oxidation product of Ag2O, respectively. (h-k) Atomistic nucleation and growth of oxide at the surface-TB junction. (h) Clean surface of the nanocrystal with alternate (111) atomic facets and kink steps, where a higher density of kink steps pre-exist near the TB. (i) Preferential surface adsorption of oxygen at the TB tip, as indicated by the red dotted curves. (j) A tiny oxide nucleus formed at the TB-surface junction. (k) The continuous growth of Ag2O along the TB, as shown by the red arrow. Scale bars: (a) and (e) 5 nm; (h) 2 nm.

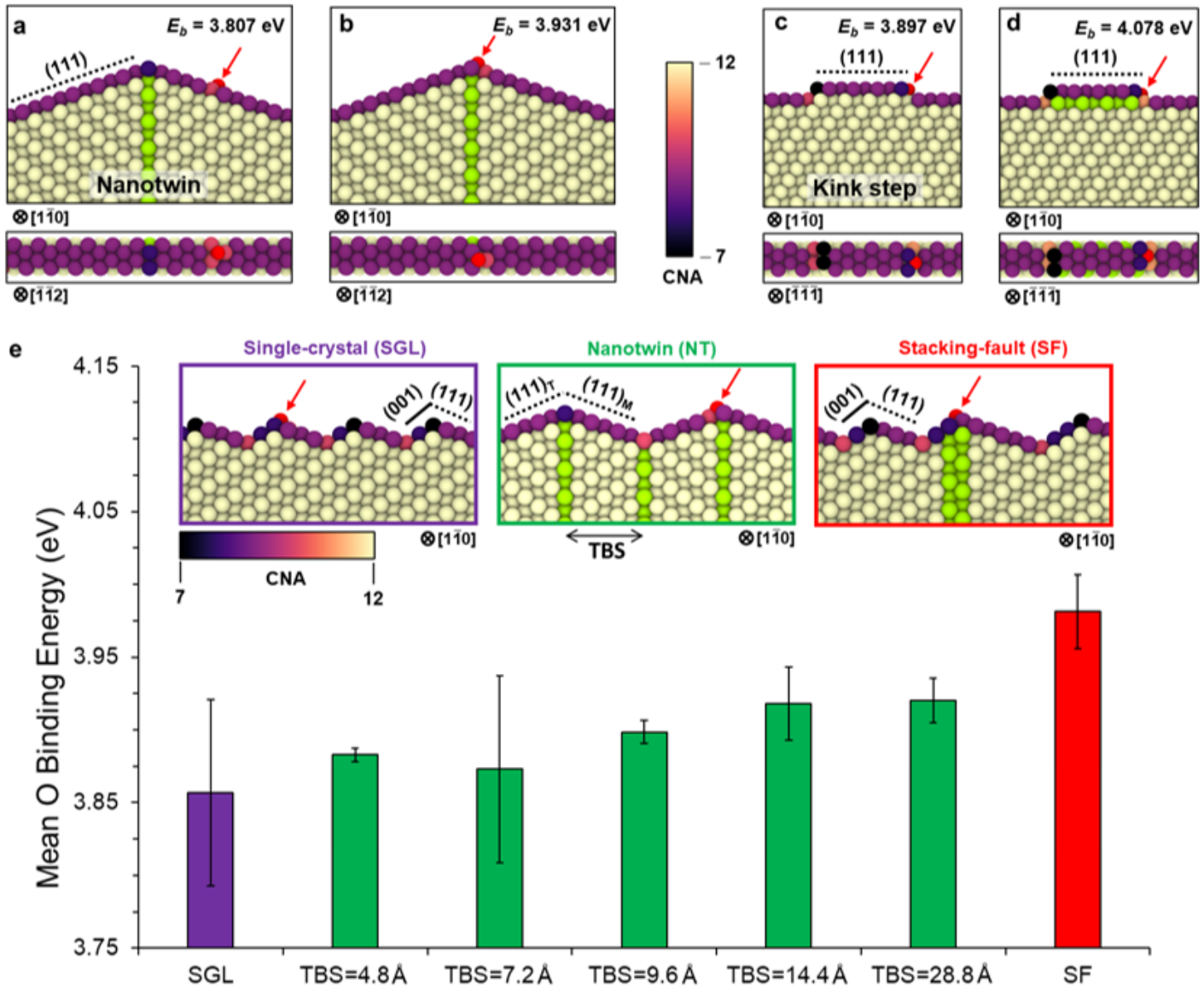

Figure 2

Density-functional-theory calculations of the Ag-O binding energy at different surface sites of single-crystal (SGL), nanotwinned (NT) and stacking-fault (SF) contained Ag. (a-b) Rise of interstitial O surface binding energy Eb closer to a twinned tip surrounded by atomically smooth {111} facets. The oxygen atom is shown in red colour. Atoms of TBs and SFs are highlighted in green and other atoms in Ag are coloured using the coordination number analysis (CNA). (c-d) Rise of Eb in SGL Ag for oxygen binding to a (111) kink step if a SF defect was hypothetically present under the surface. (e) Mean oxygen binding energy at different surface sites of SGL, TB and SF in Ag nanocrystals, where the twin-boundary spacing (TBS) is varied from 4.8 Å to 28.8 Å. The highest mean O binding energy is predicted to occur near isolated TBs (TBS = 28.8 Å) and SFs. The different surface configurations are shown in the insets, where the (001) and (111) surface facets are delineated with solid and dashed lines, respectively.

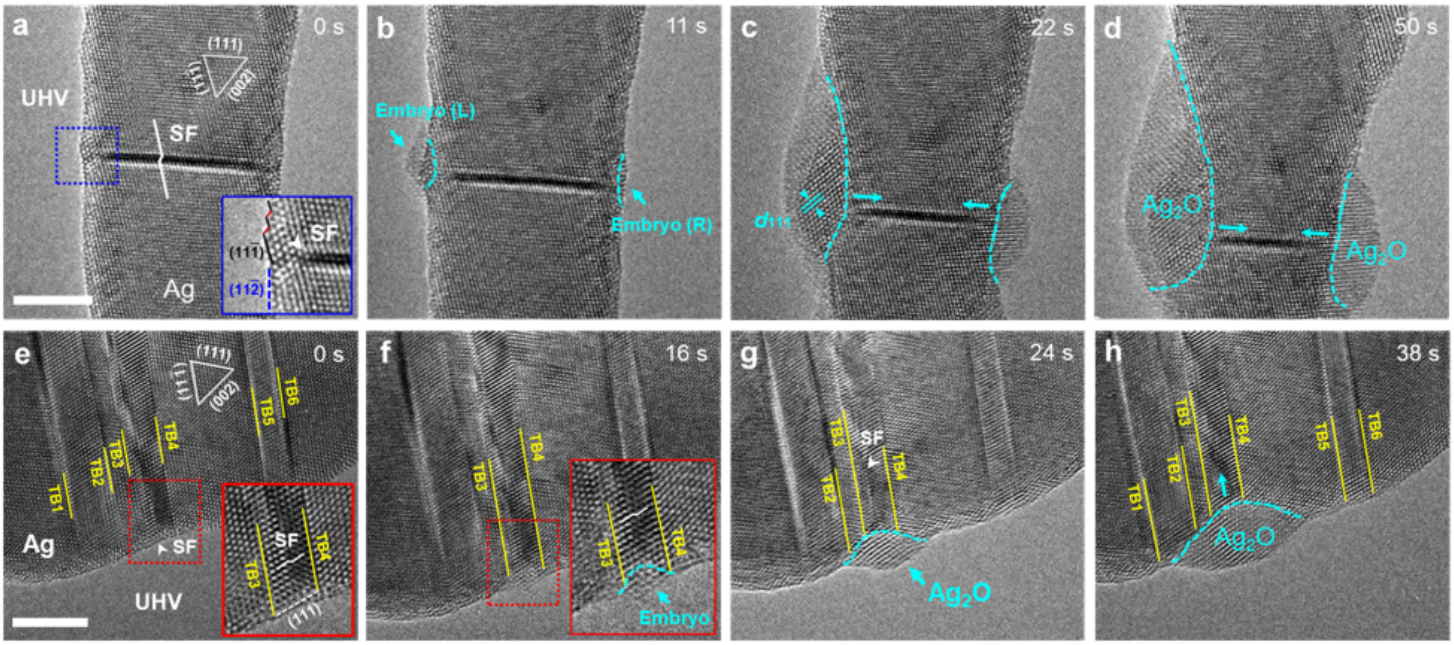

Figure 3

Selective oxidation of Ag nanocrystals containing unevenly spaced planar defects. (a-d) Preferential oxidation of an Ag nanocrystal with an isolated SF. The oxide nucleated preferentially from the SF-surface junctions on both sides, as indicated by the light blue arrows (a-b), followed by SF-assisted inward and lateral growth of Ag2O island (c-d). Inset in (a) shows the atomistic structure of the surface near the SF, which consists of atomically-flat (11"2‾) plane and several (11"1‾) kink steps. (e-h) Preferential oxidation in an Ag nanocrystal with unevenly spaced planar defects. (e) Multiple parallel TBs (#1-6) and a SF (indicted by the white arrow) pre-existed in the as-fabricated Ag nanocrystal with clean surfaces. (f) Oxide embryo nucleated preferentially at the SF-surface junction. (g) Inward growth of the Ag2O island along the same SF plane. (h) Integrated inward and lateral growth of the Ag2O oxide with the annihilation of the SF. No oxidation was observed at other TB-surface intersection sites. Insets in (e-f) are zoomed-in snapshots presenting the atomistic nucleation of the oxide embryo at the SF-(111) surface facet junction. Scale bars: (a) and (e) 5 nm.

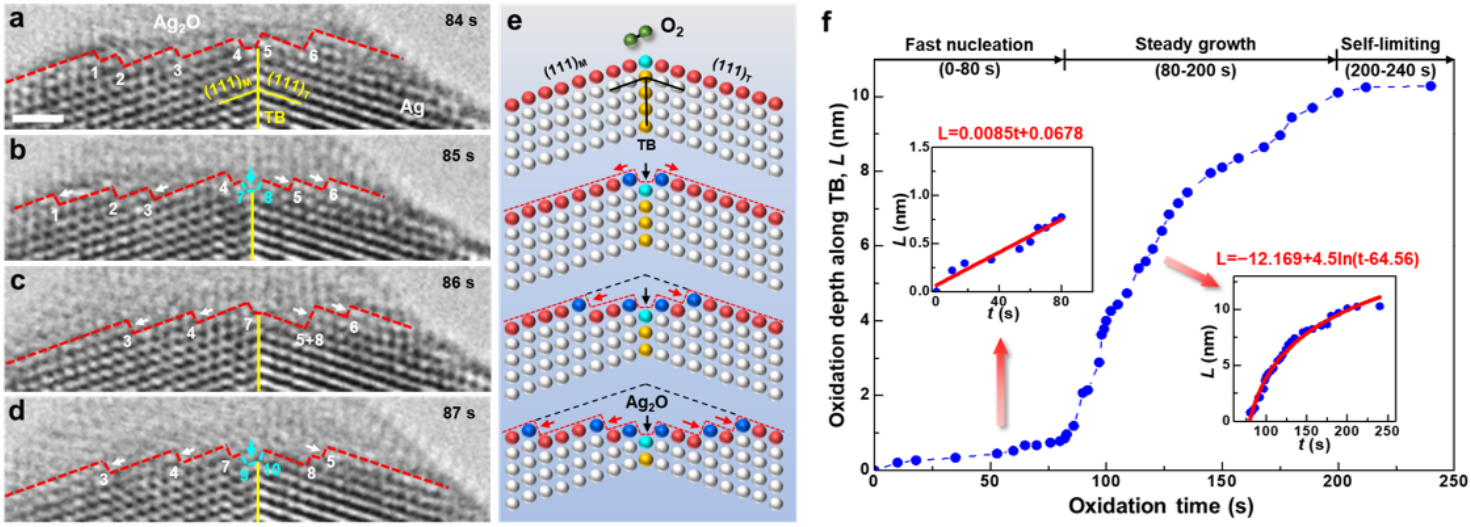

Figure 4

Dynamics of TB-assisted oxidation in Ag nanocrystal. (a) The sharp reaction interface with atomic steps (denoted as 1-6 respectively) between the Ag matrix and the as-formed Ag2O. (b) Inward oxidation along the TB, as shown by the dissolution of atoms at the TB tip (pointed out by the aqua arrow) into the oxide (Ag2O), which induces two new atomic steps (denoted as 7 and 8, respectively). (c-d) Consecutive nucleation of interphase steps from the TB junction, which migrate laterally along the conjugate (111) facets, leading to layer-by-layer oxidation of the Ag nanocrystal. (e) Schematic showing the layer-by-layer mechanism of TB-assisted oxidation in nanotwinned Ag. The atom columns at the TB tip, interphase steps, and interface terraces are coloured aqua, dark blue, and red, respectively. (f) The time-dependent inward oxide growth (characterized by oxidation depth, L) along TB in the Ag nanocrystal presented in Fig. 1. The oxidation depth-time plot was obtained by measuring the distance between the original surface-TB junction and the advancing interface-TB junction. Insets are the mathematical fitting of time-dependent oxide growth during different stages. Scale bar: 1 nm.

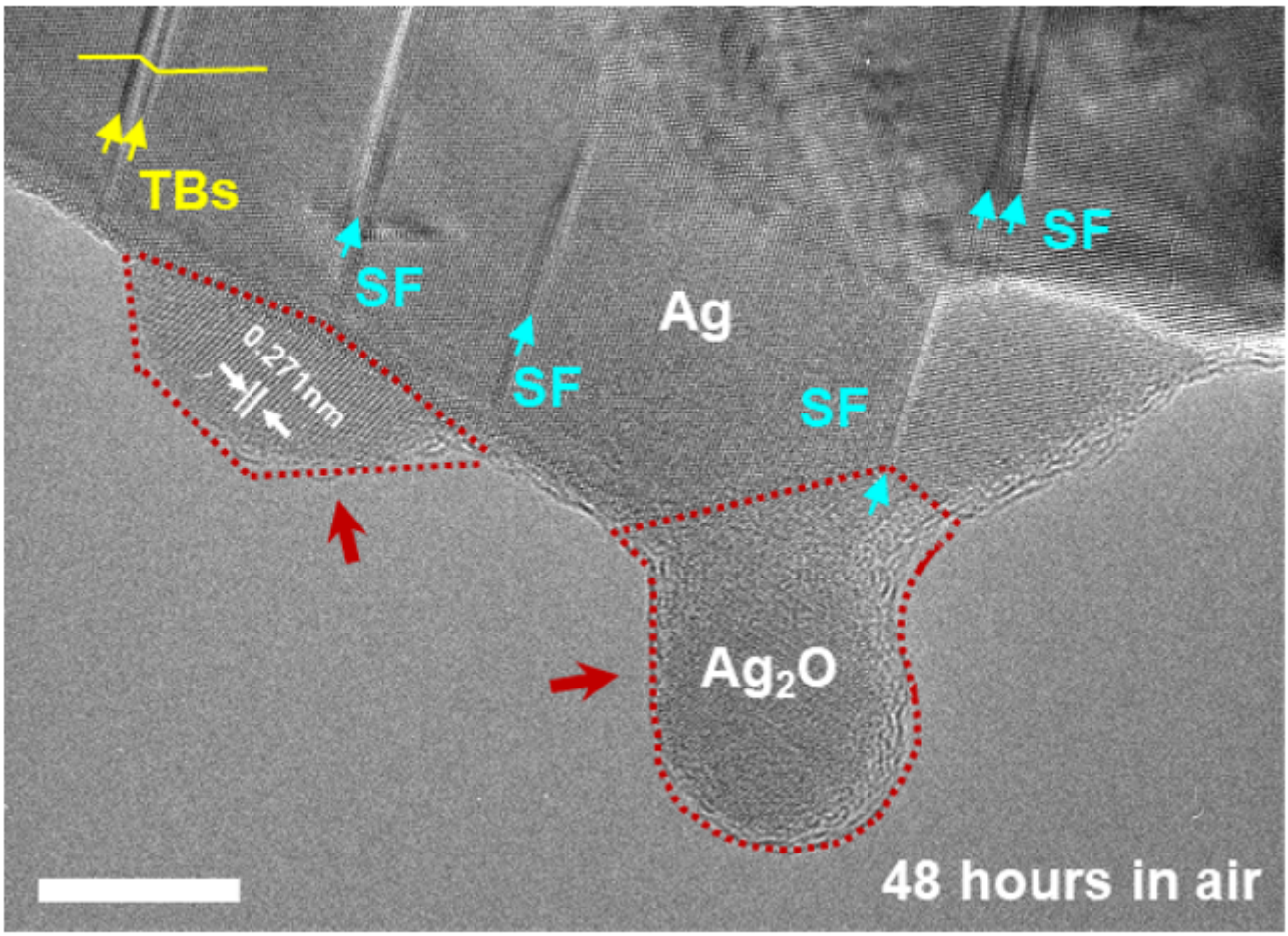

Figure 5

Natural oxidation of Ag nanocrystal with multiple planar defects. The Ag nanocrystal was exposed in ambient air at room temperature for two days. The naturally oxidized Ag also exhibits similar site-selective inward oxidation behaviour along the pre-existing SFs. Scale bar: 10 nm.

Supplementary Files

This is a list of supplementary files associated with this preprint. Click to download.

- SI.docx